



Research paper

## Rational utilization of highly conductive, commercial Elicarb graphene to advance the graphene-semiconductor composite photocatalysis



Kang-Qiang Lu<sup>a,b</sup>, Yan Chen<sup>a,b</sup>, Xin Xin<sup>a,b</sup>, Yi-Jun Xu<sup>a,b,\*</sup>

<sup>a</sup> State Key Laboratory of Photocatalysis on Energy and Environment, College of Chemistry, Fuzhou University, Fuzhou 350116, PR China

<sup>b</sup> College of Chemistry, New Campus, Fuzhou University, Fuzhou 350116, PR China

### ABSTRACT

Graphene oxide (GO) has widely been used as the precursor of graphene to construct graphene-semiconductor composite photocatalysts for various redox reactions. However, the electrical conductivity and charge carrier mobility of reduced GO (RGO) are remarkably decreased due to considerable disruption of the 2D  $\pi$ -conjugation of the electronic structure in the domain of RGO sheets, which results that the net improvement efficiency of photoactivity is often limited. Herein, we report a simple yet efficient strategy of rational utilization of highly conductive, commercial Elicarb graphene (EGR), which is manufactured on a large scale via a high-shear exfoliation process in liquid phase, to synthesize EGR-semiconductor CdS composite photocatalysts with distinctly enhanced activity as compared to RGO-CdS counterparts for photocatalytic hydrogen evolution under visible light illumination. To resolve the low solution processability deficiency of EGR, we select the surfactant, sodium dodecyl benzene acid (SDBS), to functionalize the surface of EGR with additional hydrophilic functional groups, thereby making SDBS-modified EGR well dispersed in aqueous phase and negatively charged. In addition, the hybridization of CdS with graphene via the electrostatic self-assembly strategy guarantees the intimate interfacial contact. This conceptual study would spur further interest in virtuous interactive loop between fundamental research and commercialization of graphene materials to advance graphene-semiconductor composite photocatalysis.

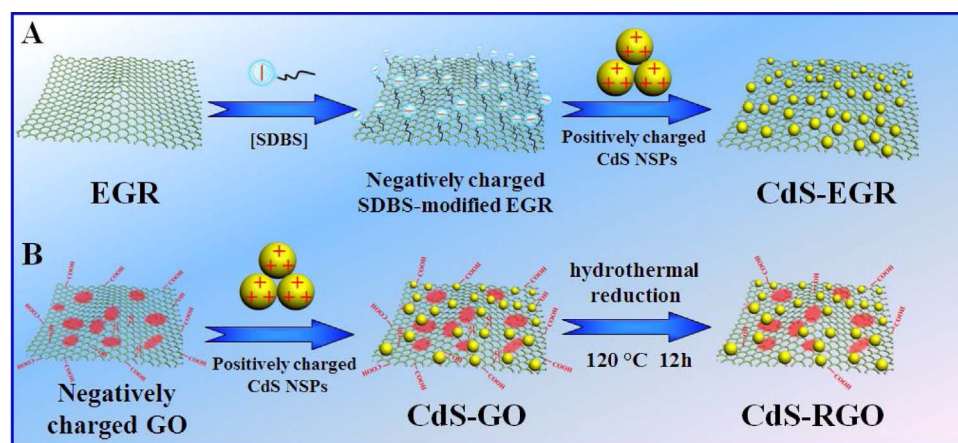
### 1. Introduction

Graphene-semiconductor composite photocatalytic systems have received ever-increasing attention due to the attractive possibilities to alleviate environmental and energy issues [1–9]. Extensive endeavors have been made to construct high-performance graphene-semiconductor composite photocatalysts for solar energy conversion [10–18]. An overview of the literature reveals that the functions of graphene in the graphene-semiconductor composite photocatalysts mainly serve as an electron reservoir to accept and transport photo-generated electrons from the semiconductors [1,19–23]. Although reduced graphene oxide (RGO) is the most frequently used electron-transfer mediator for constructing graphene-based composite photocatalysts due to its simple fabrication procedure and amenable wet-chemistry processability, the intrinsic population of structural defects result in considerable disruption of the 2D  $\pi$ -conjugation of electronic structure of graphene, leading to its much lower electrical conductivity than that of defect-free, non-oxygenated graphene and significantly hindering the photoexcited electron transfer and charge carriers

separation [1,18,24–28]. Therefore, the employment of high-quality graphene with superior electronic conductivities would be a straightforward strategy for improving the performance of graphene-semiconductor composite photocatalysts.

Chemical vapor deposition (CVD) is an efficient method to prepare pristine graphene with high electrical conductivity [29,30]. However, chemical vapor deposition of precursor gases (e.g., CH<sub>4</sub>, H<sub>2</sub>) require high temperature and complicated transfer processes, which is not suitable for convenient mass production of high quality graphene [31,32]. Directly exfoliating natural graphite flakes through sonication in organic solvents is another common method to synthesize defect-few or defect-free graphene with high quality [33–35]. However, it is usually in a very limited way that only the surface layers of graphite are peeled off, and the actual yield of exfoliated graphene is very low [18,31,36]. Fortunately, with strenuous research and entrepreneurial efforts, significant progress towards innovative graphite exfoliation methods for manufacturing high-quality graphene layers on a large scale has been achieved and the commercialization of high-quality graphene has also been realized in recent years [31,37]. In 2014,

\* Corresponding author at: State Key Laboratory of Photocatalysis on Energy and Environment, College of Chemistry, Fuzhou University, Fuzhou 350116, PR China.  
E-mail address: [yjxu@fzu.edu.cn](mailto:yjxu@fzu.edu.cn) (Y.-J. Xu).



**Scheme 1.** Schematic representation of the preparation of CdS-EGR (A) and CdS-RGO composites (B) based on the electrostatic self-assembly strategy.

chemical company Thomas Swan has developed a simple and scalable manufacturing method *via* a liquid-phase, high-shear exfoliation process to produce high-quality graphene with superior electrical conductivity [38,39]. In the second half of 2014, Thomas Swan & Co. Ltd. has begun producing and selling graphene under the commercial name Elicarb from its initial pilot plant affording 1 kg of product per day [37]. Therefore, direct utilization of the high-quality, commercial graphene would be a feasible approach to construct graphene-semiconductor composite photocatalysts with improved activity, because in principle such highly conductive graphene is able to serve as the better co-catalyst of electrons mediator. Consequently, it is of significant interest to investigate how to utilize the highly conductive commercial Elicarb graphene (EGR) to construct more efficient graphene-based composite photocatalysts.

Herein, by taking the semiconductor CdS as an example, we have synthesized a series of CdS-graphene (EGR and RGO) composite photocatalysts with different weight addition ratios of graphene, during which the surface modification of using the surfactant of sodium dodecyl benzene acid (SDBS) is adopted to resolve the low solution processability deficiency of EGR and increase the compatibility of EGR with CdS in the wet-chemistry synthesis process. In addition, the electrostatic self-assembly strategy not only enables the good interfacial contact during the hybridization of semiconductor CdS and the graphene sheets, but also maintains the original morphology of CdS in a uniform manner that excludes the effect of morphology difference of CdS on the photocatalytic performance of CdS-graphene composites. Direct comparison under identical reaction conditions suggests that the CdS-EGR composites exhibit much higher photocatalytic hydrogen evolution activity than CdS-RGO. The characterization results indicate that the improved electrical conductivity of EGR as compared to RGO results in the significant enhancement of separation and transfer efficiency of charge carriers photogenerated from semiconductor CdS under visible light irradiation, which consequently contributes to photoactivity improvement. It is expected that this work could open up new frontiers for advancing the rational utilization of highly conductive commercial graphene to synthesize more efficient graphene-based composite photocatalysts, which might bring the commercial graphene materials closer to real-world applications in artificial redox processes.

## 2. Experimental

### 2.1. Materials

All reagents were analytical grade and used without further purification. Cadmium acetate dihydrate ( $\text{Cd}(\text{CH}_3\text{COO})_2 \cdot 2\text{H}_2\text{O}$ ), thiourea ( $(\text{NH}_2\text{CSNH}_2$ )), (3-aminopropyl)-triethoxysilane ( $\text{C}_9\text{H}_{23}\text{NO}_3\text{Si}$ , APTES), sulfuric acid ( $\text{H}_2\text{SO}_4$ ), hydrochloric acid (HCl), hydrogen peroxide, 30% ( $\text{H}_2\text{O}_2$ ), potassium permanganate ( $\text{KMnO}_4$ ), sodium dodecyl benzene

sulfonate (SDBS) and ethanol ( $\text{C}_2\text{H}_6\text{O}$ ) were obtained from Sinopharm Chemical Reagent Co., Ltd. (Shanghai, China). Graphite powder was supplied from Qingdao Zhongtian Company, China. Elicarb graphene (EGR) was obtained from Thomas Swan Co. Ltd. (UK); Deionized water used in the synthesis was from local sources.

### 2.2. Synthesis

#### 2.2.1. Fabrication of uniform CdS nanospheres (CdS NSPs) and APTES treated CdS NSPs

Uniform CdS NSPs were obtained through a facile hydrothermal method [40,41]. The detail of the typical process was presented in the Supporting Information. The APTES treated CdS NSPs was performed as follows. Typically, 0.4 g CdS NSPs was first dispersed in 200 mL of ethanol by sonication for 30 min. Then, APTES (2 mL) was added, heated in 60 °C, and refluxed for 4 h. For reference, the structural formula of APTES was displayed in the Supporting Information. The products were cooled to room temperature and recovered by filtration, washed with ethanol, and fully dried at 60 °C in an oven to get the final positively charged APTES treated CdS NSPs.

#### 2.2.2. Synthesis of graphene oxide (GO)

GO was synthesized from natural graphite powder by a modified Hummers' method [7,8,11,42–46]. The detailed procedure was described in the Supporting Information.

#### 2.2.3. Synthesis of CdS-EGR and CdS-RGO composites

For the synthesis of CdS-EGR composites, as shown in Scheme 1A, the EGR was firstly modified with the SDBS to enhance its water solubility and render it negatively charged. The structural formula of SDBS was displayed in the Supporting Information. Typically, 10 mg EGR was dispersed in 50 mL of 0.1 M SDBS aqueous solution. The mixture was sonicated for 2 h, and mixed for 3 h at room temperature under mild stirring. Then, the solution was filtered and rinsed with deionized water to wash away the redundant SDBS, obtaining the negatively charged SDBS-modified EGR. After that, the negatively charged SDBS-modified EGR was added into the positively charged APTES treated CdS NSPs dispersion at the weight ratio of EGR to CdS NSPs at 0.005:1, 0.01:1, 0.02:1, 0.04:1 and 0.05:1 under vigorous stirring at pH = 6. After mixing for 12 h, the mixture was then filtered, washed until the pH of rinse water became neutral, and fully dried at 60 °C in an oven to get the final CdS-EGR composites with different weight addition ratios of EGR, namely CdS-0.5, 1, 2, 4 and 5% EGR. For comparison, the synthesis process of CdS-RGO composites using GO as the precursor of RGO was shown in Scheme 1B. The negatively charged GO suspension was added into a positively charged APTES treated CdS NSPs dispersion at the weight ratio of GO to CdS NSPs at 0.005:1, 0.01:1, 0.02:1, 0.04:1 and 0.05:1 under vigorous stirring at pH = 6. After mixing for 12 h, the

mixture was centrifuged and washed with deionized water. For the reduction of GO, a hydrothermal process was used as follows. CdS NSPs/GO (0.1 g) composites with different weight addition ratios of GO were dispersed in deionized water (80 mL) and then autoclaved in a 100 mL Teflon-lined stainless steel vessel at 120 °C for 12 h. Next, the products were cooled to room temperature and recovered by filtration, washed by water, and fully dried at 60 °C in an oven to obtain the final CdS-RGO composites with different weight addition ratios of RGO, namely, CdS-0.5, 1, 2, 4 and 5% RGO composites.

### 2.3. Characterizations

X-ray photoelectron spectroscopy (XPS) analysis was completed on a Thermo Scientific ESCA Lab 250 spectrometer equipped with a mono chromatic Al K $\alpha$  (X-ray source), a multiaxial sample stage and a hemispherical analyzer. The calibration of the binding energies was based on the C 1s peak at 284.6 eV. A Nanoscope IIIA system was used to measure the atomic force microscopy (AFM) spectra. X-ray diffractometer (Philip X' Pert Pro MPP) with Ni-filtered Cu K $\alpha$  radiation ( $\lambda = 1.5418 \text{ \AA}$ ) was employed to collect the X-ray diffraction (XRD) spectra of the samples. Ultraviolet-visible (UV-vis) diffuse reflectance spectra (DRS) were recorded on a Cary-500 UV-vis-NIR spectrometer in which BaSO<sub>4</sub> powder was used as the internal standard to obtain the optical properties of the samples. Zeta-potentials ( $\zeta$ ) measurement in deionized water was determined by dynamic light scattering analysis (Zetasizer 3000HSA) at room temperature. Scanning electron microscopy (SEM, FEI Nova NANOSEM 230) and transmission electron microscopy (TEM, FEI Tecnai G2 F20 S-TWIN) were used to determine the morphology and microscopic structure of the samples. The electrical conductivity measurement of graphene (RGO and EGR) was performed by measuring the resistivity-pressure curve (R-P curve) using a four-point probe technique on a ST2722 (Suzhou Jingge Electronic Co., P. R. China) power resistivity tester. A Renishaw inVia Raman System 1000 with a 532 nm Nd:YAG excitation source was employed to collect the Raman spectra at room temperature. The nitrogen adsorption-desorption isotherms and Brunauer-Emmett-Teller (BET) surface areas were measured on a Micromeritics ASAP2010 equipment. The photoluminescence spectra (PL) for powder samples were analyzed on an Edinburgh Analytical Instrument F900 spectrophotometer with an excitation wavelength of 420 nm. To ensure the comparability of the PL spectra, the experimental parameters, including the excitation wavelength, slit width, and the amount of the samples, were identical. The contact angle of the prepared membranes was analyzed using a contact angle goniometer (OCA-20, Dataphysics, Germany). The concentration of the leached Cd<sup>2+</sup> in solution was quantified by an inductively coupled plasma emission spectroscopy instrument (ICP, PerkinElmer Optima 2000DV)

Photoelectrochemical measurements were performed in a homemade three electrode quartz cell with a PAR VMP3 Multi Potentiostat apparatus. A Pt plate was used as the counter electrode, and Ag/AgCl electrode was used as the reference electrode. The working electrode was prepared on fluorine-doped tin oxide (FTO) glass that was cleaned by ultrasonication in ethanol for 30 min and dried at 80 °C. Typically, 5 mg of the sample powder was ultrasonicated in 0.5 mL of ethanol to disperse it evenly to get a slurry. The slurry was spread onto FTO glass, whose side part was previously protected using Scotch tape. After air drying, the working electrode was further dried at 100 °C for 2 h to improve adhesion. Then, the Scotch tape was unstuck, and the uncoated part of the electrode was isolated with epoxy resin. The exposed area of the working electrode was 0.25 cm<sup>2</sup>. The electrochemical impedance spectroscopy (EIS) measurement was carried out using a CHI-660D workstation, (CH Instrument, USA) in the three electrode cell in the presence of 0.5 M KCl solution containing 0.01 mM K<sub>3</sub>[Fe(CN)<sub>6</sub>]/K<sub>4</sub>[Fe(CN)<sub>6</sub>] (1:1) under open circuit potential conditions. The photocurrent measurement was carried out on a BAS Epsilon workstation without bias and the electrolyte was 0.2 M aqueous Na<sub>2</sub>SO<sub>4</sub> solution (pH = 6.8)

without an additive. The visible light irradiation source was a 300 W Xe arc lamp system equipped with a UV-CUT filter ( $\lambda > 420 \text{ nm}$ ). The cathodic polarization curves were obtained using the linear sweep voltammetry (LSV) technique with a scan rate of 0.2 mV s<sup>-1</sup>.

### 2.4. Photocatalytic H<sub>2</sub> evolution

The photocatalytic H<sub>2</sub> evolution was performed in a Pyrex reaction cell connected to a closed gas circulation and evacuation system. In a typical photocatalytic experiment, 40 mg of the prepared photocatalysts was dispersed with constant stirring in an 80 mL mixed solution of water (72 mL) and lactic acid (8 mL), which has been well proven to be a good hole scavenger without obvious influence on the origin of the produced H<sub>2</sub> [16,42,47]. Prior to irradiation, the solution was degassed for 20 min, followed by irradiation with a 300 W Xe arc lamp (PLS-SXE 300C, Beijing Perfectlight Co., Ltd.) equipped with a filter to cut off light of wavelength below 420 nm ( $\lambda > 420 \text{ nm}$ ), and the intensity of visible light irradiation was about 4.5 kW m<sup>-2</sup>. The reactant solution was stirred and maintained at low temperature by a flow of cooling water during the photocatalytic reaction. The evolved H<sub>2</sub> was *in situ* monitored periodically by an online gas chromatograph with a thermal conductivity detector (Shimadzu GC-8A, argon as a carrier gas and MS-5A column). The recycling test of catalytic H<sub>2</sub> evolution over the as-prepared photocatalyst was done as follows. Typically, after the reaction of the first run under visible light irradiation, the photocatalyst was separated by filtration and washed with deionized water three times. Then, the fresh reaction solution of 80 mL of lactic acid aqueous solution (10 vol%) was mixed with this used catalyst to subject it to the second run photocatalytic activity test. The subsequent three runs of photocatalytic recycling tests were performed in a similar manner. The apparent quantum efficiency (AQE) of H<sub>2</sub> evolution was conducted under the same photocatalytic conditions. The 300 W Xe lamp equipped with a 420 nm band-pass filter was used as the light source, and the number of incident photons was measured using a radiant power energy meter (Ushio spectroradiometer, USR-40). The apparent quantum efficiency (AQE) was calculated according to the equation as the following:

$$\begin{aligned} \text{AQE} &= \frac{\text{Number of reacted electrons}}{\text{Number of incident photons}} \times 100\% \\ &= \frac{\text{Number of evolved H}_2 \text{ molecules} \times 2}{\text{Number of incident photons}} \times 100\% \end{aligned}$$

## 3. Results and discussion

**Fig. 1A** shows the typical Raman spectra of GO and EGR. Of particular note is the intensity ratio of the D and G bands, I<sub>D</sub>/I<sub>G</sub>, which is a measure of the relative concentration of local defects or disorders (particularly the sp<sup>3</sup> hybridized defects) compared to the sp<sup>2</sup> hybridized graphene domains [33,46]. As can be seen clearly, the I<sub>D</sub>/I<sub>G</sub> ratio is 0.14 for EGR, which is remarkably lower than 1.01 for GO. This indicates the much lower defects density of EGR than GO. The other structural feature is that, for EGR, the amount of surface oxygenated functional groups is significantly lower than that for GO, which can be reflected by the direct comparison of C 1s spectra between EGR and GO as displayed in **Fig. 1B** and C. In addition, from the photograph as shown in **Fig. 1D**, we can see that the color of GO and EGR dispersions in water is remarkably different. In particular, the GO dispersion in water exhibits a brilliant yellow color, which indicates the richness of oxygenated functional groups on the surface of GO [8,44]. The abundance of hydrophilic functional groups on the GO surface makes it act as “a big macromolecular surfactant” well dispersed in an aqueous phase [35]. Furthermore, as shown in **Fig. S1A**, these oxygenated functional groups render the surface of GO negatively charged, which establishes an efficient basis for electrostatic attraction with the positively charged CdS nanospheres (CdS NSPs) [40,48]. However, when

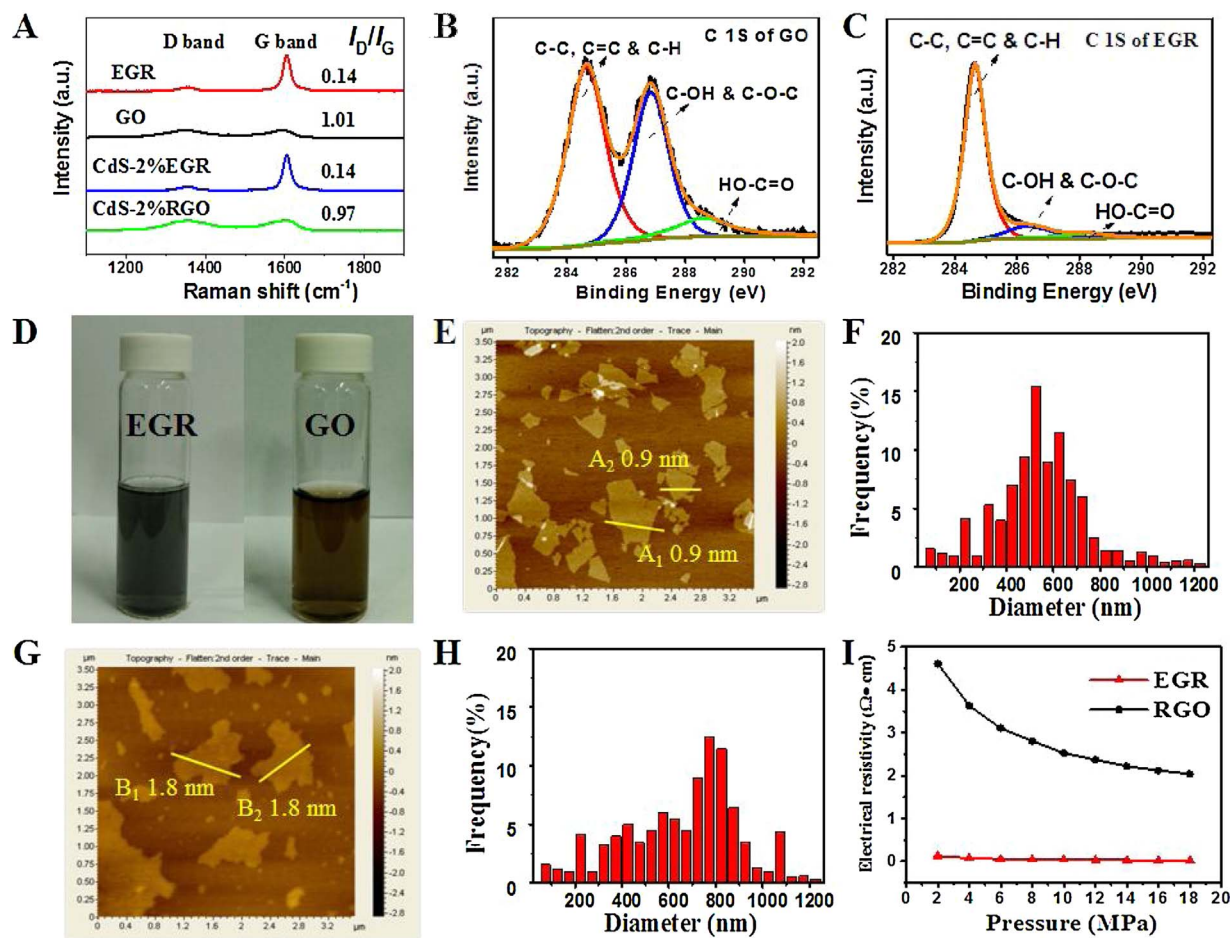


**Fig. 1.** Raman spectra of GO, EGR, CdS-2%RGO and CdS-2%EGR (A); XPS spectra of C 1s of GO (B) and EGR (C); photograph of GO and EGR (D); AFM spectra, size distribution and height profiles taken along the yellow line of the original GO (E,F) and EGR (G,H); and the resistivity-pressure (R-P) curves of RGO and EGR (I). (For interpretation of the references to colour in this figure legend, the reader is referred to the web version of this article.)

EGR has been used instead of GO dispersed in water, EGR is not able to behave as a “GO-like” macromolecular surfactant possessing excellent water solubility and effectively attract the positively charged CdS NSPs onto its giant 2D surface *via* the electrostatic interaction. In order to resolve this deficiency, a moderate amount of anionic surfactant, *i.e.*, sodium dodecyl benzene acid (SDBS) is introduced to functionalize the surface of EGR. As an amphiphilic molecule, SDBS contains long alkyl chain (dodecyl-C<sub>12</sub>H<sub>25</sub>), which gives its hydrophobic nature and the benzenesulphonate (C<sub>6</sub>H<sub>5</sub>SO<sub>3</sub><sup>-</sup>) group is responsible for its hydrophilic character [49]. The hydrophobic part of the SDBS can be conjugated onto the planar graphene *via* hydrophobic interactions, while the hydrophilic part is capable of improving SDBS-modified EGR dispersibility in water [50,51]. As shown in Fig. S2A, after storage for at least two months, the SDBS-modified EGR dispersion was still very homogenous and stable. In contrast, the EGR dispersion without functionalization contains coagulated architectures at the bottom of vial (Fig. S2B). Furthermore, the hydrophilicity of the samples has also been investigated by water contact angle measurement. Lower contact angle indicates that the membrane surface is more hydrophilic in nature [52,53]. As shown in Fig. S3, while a big contact angle of 74.5° is observable for the EGR membrane, the SDBS-modified EGR membrane shows a much smaller contact angle of 51.8°, reflecting the higher surface hydrophilicity of SDBS-modified EGR than original EGR. Importantly, as shown in Fig. S1B, this slight modification not only enhances the hydrophilicity of EGR, but also makes the surface of SDBS-modified EGR negatively charged. Consequently, the negatively charged SDBS-modified EGR can be easily assembled with positively charged CdS NSPs through the electrostatic attraction [54].

Fig. S4 shows the typical scanning electron microscopy (SEM) images of GO and EGR, it can be seen that both the GO and EGR exhibit the unique ultrathin two-dimensional structure and clean surface. The atomic force microscopy (AFM) has been used to obtain detailed information about the average lateral size and thickness of GO and EGR sheets. As shown in Fig. 1E–H, the results indicate that GO and EGR sheets possess similar lateral size, which varies from 0.3 to 1.3  $\mu\text{m}$ . The corresponding height profiles in Fig. S5 show that the GO sheets exhibit an apparent thickness about 0.9 nm, which corresponds to the thickness of monolayer of graphene and the apparent thickness of EGR sheets is predominantly about 1.8 nm, corresponding to the bilayer graphene [44,55,56]. Furthermore, the four-point probe technique has been employed to investigate the electrical conductivity of graphene (EGR and RGO). As shown in Fig. 1I, under the pressure range of 2–20 MPa, the resistivity-pressure (R-P) curves of the EGR and RGO samples show that the resistivity of EGR is much lower than that of RGO. Since that the electrical conductivity is the inverse of resistivity (1/R), the result clearly demonstrates that the electrical conductivity of EGR is obviously much higher than that of RGO [44]. Furthermore, the resistivity test as shown in Fig. S6 clearly suggests that the SDBS modification has a negligible effect on the electrical conductivity of EGR. Such an enhanced electronic conductivity of the EGR sheets would be beneficial for the transfer process of photogenerated charge carriers across the interfacial domain between graphene and semiconductor, which thus improves the photocatalytic activity of graphene-semiconductor composites [1,10,35,44,57,58].

A series of CdS-RGO and CdS-EGR composites with different weight addition ratios of graphene (RGO or EGR) have been fabricated *via* a

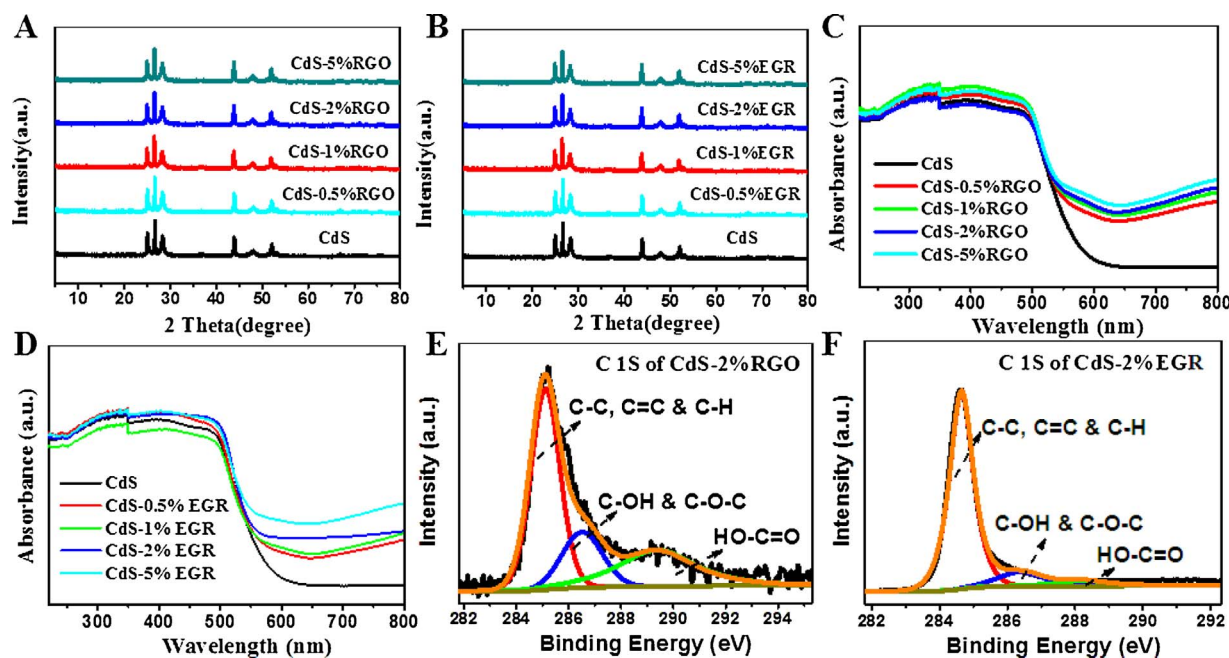


**Fig. 2.** XRD patterns and UV-vis DRS of CdS, CdS-RGO composites with different weight ratios of RGO (A, C) and CdS-EGR composites with different weight ratios of EGR (B, D). XPS spectra of C 1s of CdS-2%RGO (E) and CdS-2%EGR (F).

simple electrostatic self-assembly strategy (Scheme 1). As shown in Fig. 2A,B, the as-prepared CdS-RGO and CdS-EGR composites possess similar X-ray diffraction (XRD) spectra. The well-resolved diffraction peaks are all in accordance with a hexagonal CdS phase [40,59]. Notably, no typical diffraction peaks of RGO or EGR are observed, which could be ascribed to the fact that relatively low diffraction intensity of RGO/EGR might be shielded by the main peak of CdS [44,57]. As shown in Fig. 2C,D, the diffuse reflectance spectra (DRS) show that the CdS-RGO and CdS-EGR samples display the analogous light absorption fingerprint. With the increased addition ratio of RGO or EGR, the enhanced light absorption of CdS-RGO and CdS-EGR from 530 to 800 nm can be attributed to the intrinsic background absorption of black colored graphene [8,46]. The similarity in XRD and DRS results suggests that the use of EGR instead of RGO has no significant influence on the crystal phase and the light absorption property for the CdS-RGO and CdS-EGR composites. Fig. 2E,F displays the C 1s X-ray photoelectron spectroscopy (XPS) spectra of CdS-2%RGO and CdS-2%EGR. In comparison with XPS spectrum of original GO in Fig. 1B, a significant loss of oxygenated functional groups is observed in CdS-2%RGO, which indicates the effective reduction of GO to RGO after the hydrothermal reduction treatment. However, it is notable that there still remain oxygenated functional groups in CdS-2%RGO, which is much higher than that in CdS-2%EGR. These residual oxygenated functional groups in CdS-2%RGO result in considerable decrease of electrical conductivity of RGO [35,58]. In addition, the CdS-2%RGO and CdS-2%EGR have also been characterized by the Raman spectroscopy (Fig. 1A). Notably, the  $I_D/I_G$  ratio is 0.97 for CdS-2%RGO, which is lower than 1.01 for GO, indicating the enhanced graphitization of the RGO resulting from the hydrothermal reduction process. Nevertheless, the  $I_D/I_G$  ratio for CdS-2%RGO is obviously higher than that for CdS-2%EGR, confirming the more defect density in RGO than that in EGR.

Fig. 3A,D and G shows SEM images of CdS NSPs, CdS-2%RGO and CdS-2%EGR composites (with optimal photocatalytic activity as examples, as discussed later). Notably, both the bare CdS NSPs and CdS NSPs in CdS-2%RGO and CdS-2%EGR composites show the uniform size and shape with an average diameter about 240 nm, which indicates that the crystallite size of CdS NSPs will not be the primary reason accounting for the photoactivity difference between CdS, CdS-2%RGO and CdS-2%EGR. In addition, it can be clearly seen that the surfaces of

CdS NSPs are intimately wrapped by the veil-like graphene (RGO or EGR) sheet, forming a core@shell like structure, which indicates that the intimate interfacial contact between CdS NSPs and graphene sheets (RGO or EGR) has been achieved via such a simple electrostatic self-assembly strategy. As shown in Fig. 3B,C, the transmission electron microscopy (TEM) images of EGR clearly demonstrate that the EGR sheet consists of a few (2–3) layers of graphene. In addition, the intimate interfacial contact between graphene and CdS NSPs has been further evidenced by the TEM analysis. As shown in Fig. 3E,F and H,I, both CdS-2%RGO and CdS-2%EGR display characteristic lattice fringe of (101) crystallographic plane of CdS NSPs. The identified graphene layers in the edge area of CdS-2%RGO and CdS-2%EGR confirm the intimate interfacial contact between CdS NSPs and graphene. Since the transfer process of charge carriers in graphene-semiconductor composites is intimately related with the interfacial interaction, it could be expected that such an intimate interfacial contact for the CdS-2%RGO and CdS-2%EGR composites would be able to favor the photogenerated charge carrier transfer process across the interface between CdS NSPs and graphene upon visible light irradiation.

The photoactivity of the CdS-RGO and CdS-EGR composites has been evaluated for photocatalytic  $H_2$  evolution from water under visible light irradiation. Fig. 4A displays the photocatalytic  $H_2$  evolution activity over the as-prepared CdS-EGR. For comparison, the photoactivity results over CdS-RGO prepared by using GO as the precursor of graphene are also shown in Fig. 4B. It can be observed that although CdS is a well-known visible light driven photocatalyst, bare CdS sample shows a relatively low photocatalytic activity with a  $H_2$  evolution rate of  $42.8 \mu\text{mol g}^{-1} \text{h}^{-1}$ , corresponding to an apparent quantum efficiency (AQE) of 0.29% at 420 nm. Notably, the optimal weight ratio of graphene for achieving the optimal photocatalytic performance is the same in both CdS-EGR and CdS-RGO samples, i.e., 2%. However, the photocatalytic activity of the two optimal samples is significantly different. The  $H_2$  evolution rate over CdS-2%EGR reaches  $359.6 \mu\text{mol g}^{-1} \text{h}^{-1}$  with AQE of 3.27% at 420 nm, which is much higher than that of the optimal CdS-2%RGO composite ( $136.3 \mu\text{mol g}^{-1} \text{h}^{-1}$ , corresponding to an AQE of 1.12% at 420 nm) under identical reaction conditions. Blank experiments performed in the absence of catalysts or visible light show no  $H_2$  production, confirming that the reaction is really driven by photocatalytic process with

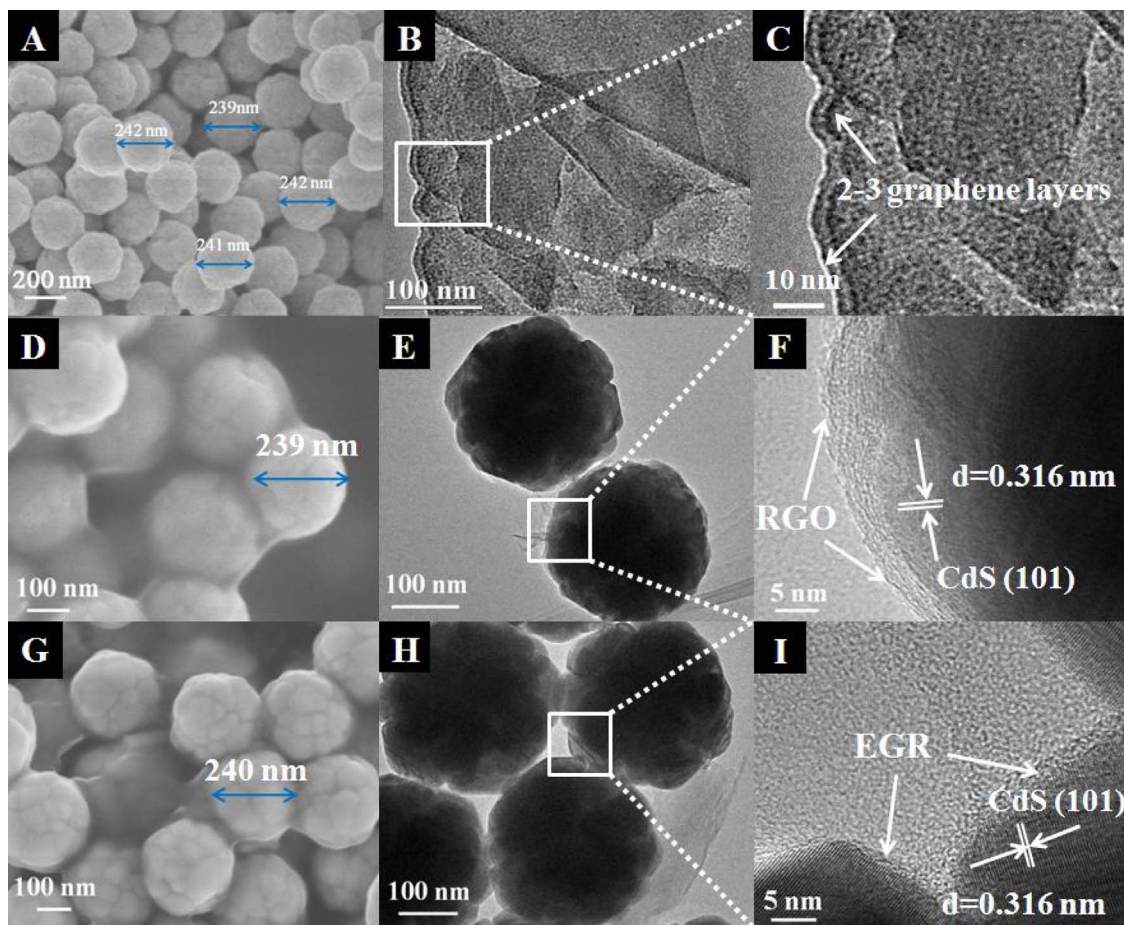


**Fig. 3.** Typical SEM images of CdS NPs (A), CdS-2%RGO (D) and CdS-2%EGR (G); TEM images of EGR (B, C), CdS-2%RGO (E, F) and CdS-2%EGR (H, I).

the assistance of catalysts. Additionally, negligible H<sub>2</sub> production is achieved using bare RGO or EGR sample under visible light irradiation (Fig. S7), suggesting that semiconductor CdS is the primary photoactive ingredient while the role of RGO or EGR acts as charge carrier dispensing co-catalyst for photocatalytic reactions [1,10,35]. In addition, time-online photoactivity test in Fig. 4C further confirms the use of the highly conductive EGR instead of RGO is a simple and efficient approach to enhance the photocatalytic H<sub>2</sub> evolution activity of CdS NSPs.

The stability is as important as activity for the practical application of semiconductor-based photocatalytic materials. To evaluate the photostability of the composites, the recycling tests over CdS, CdS-2%RGO and CdS-2%EGR have been measured as displayed in Fig. 4D. The result shows that after five cycles for 20 h of visible light irradiation, the H<sub>2</sub> evolution amounts over the CdS-2%RGO and CdS-2%EGR composites remain relatively stable; the photoactivity deterioration is lower than 15%. The results of XRD have also evidenced that there is no detectable change in the bulk properties of the fresh and recycled CdS-2%RGO and CdS-2%EGR (Fig. S8). In sharp contrast, the H<sub>2</sub> evolution activity of blank CdS has deteriorated by ca. 68%, displaying a significant photoactivity declination after five cycles, as shown in Fig. S9. Similar results have further been confirmed by the long-term chronamperometry measurement. As shown in Fig. S10, under visible light irradiation for nearly 20 h, the photocurrent density of CdS-2%RGO and CdS-2%EGR keeps relatively stable, but obvious decline of photocurrent density can be observed on blank CdS. In addition, as shown in Table S1, ICP analysis of the reaction solution of CdS-2%EGR and CdS-2%RGO after continuous visible light irradiation of 20 h shows a Cd<sup>2+</sup> leaching of about 5.9% and 6.3% (Table S1), which is close to the value of CdS-2%EGR for stirring in the dark of 20 h (5.4%). The similar leaching of Cd<sup>2+</sup> could be ascribed to the partial dissolution of the CdS

ingredient at the acidic conditions due to the presence of lactic acid [42]. The result further confirms the good photostability and strong anti-photocorrosion of CdS-graphene composites. Furthermore, the ICP analysis of the reaction solution of blank CdS after visible light irradiation of 20 h has also been performed. The Cd<sup>2+</sup> leaching has been determined to be 18.5%, which is significantly higher than that of CdS-graphene composites, indicating that the cocatalyst of graphene as a protective layer can effectively prevent CdS from photocorrosion under light irradiation. The above results clearly indicate that incorporation of CdS with graphene not only increases the photocatalytic activity but also enhances the photostability of CdS. In particular, EGR with superior electrical conductivity is more beneficial than RGO for improving the photoactivity of CdS NSPs.

The introduction of graphene (EGR or RGO) into the matrix of semiconductors CdS NSPs mainly aims to improve the photocatalytic performance of composites via harnessing the co-catalyst role of graphene to boost the separation and transfer of charge carriers photo-generated from CdS NSPs, which is the critical step for photocatalytic reactions. Because EGR displays remarkably higher electronic conductivity than RGO as discussed above, it can be deduced that for the CdS-EGR composites, EGR would better help to facilitate the separation/transfer of photogenerated charge carriers from band-gap photo-excitation of CdS NSPs under visible light irradiation, which thus contributes to the enhancement of photocatalytic activity. The subsequent comparative analyses of photoelectrochemical and photoluminescence (PL) spectra on blank CdS, CdS-2%RGO and CdS-2%EGR samples confirm this inference. Fig. 5A shows a comparison of the photocurrent-time (I-t) curves for blank CdS, CdS-2%RGO and CdS-2%EGR with typical on-off cycles of intermittent visible-light irradiation. It can be seen that the transient photocurrent response for CdS-2%RGO is higher than

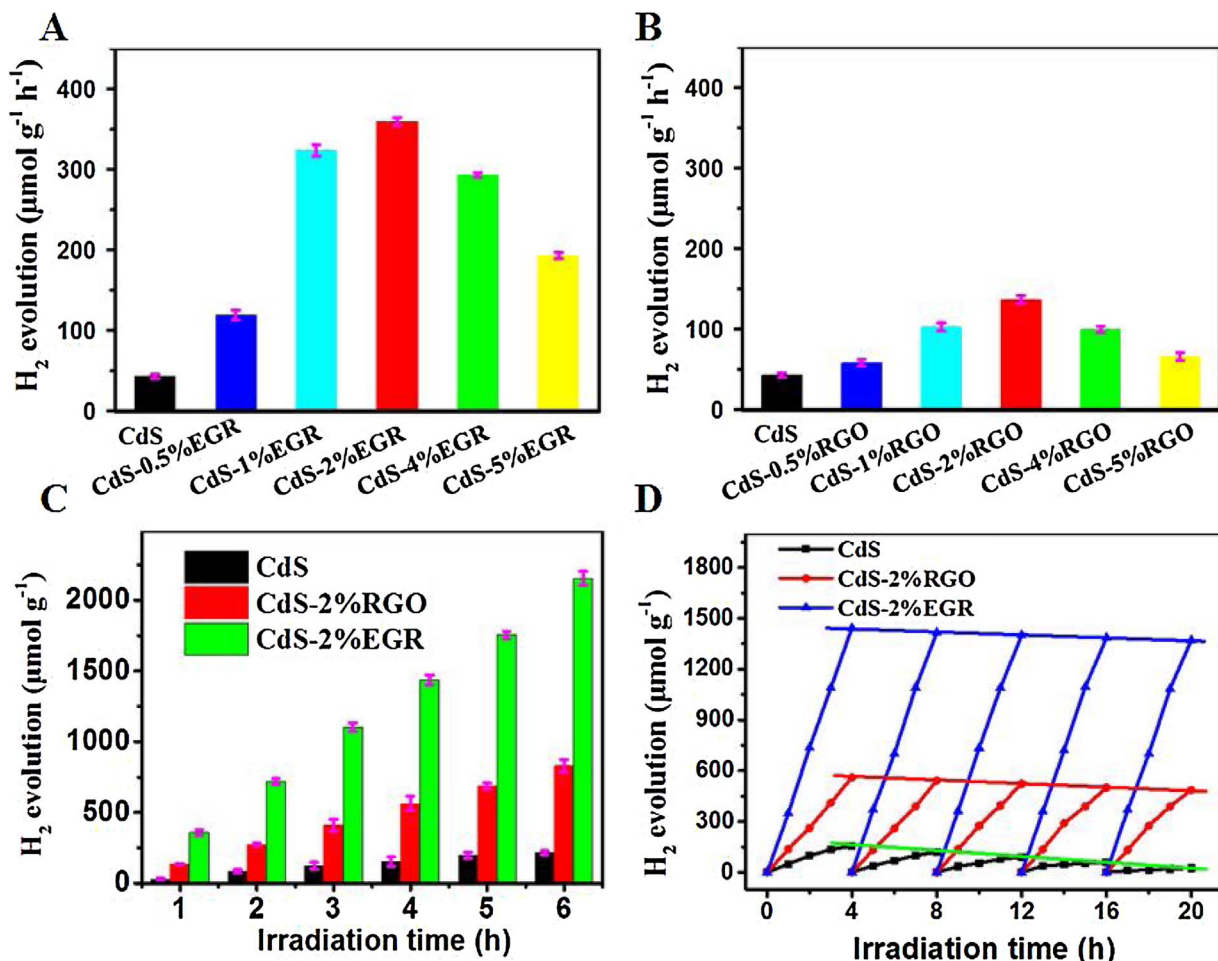


**Fig. 4.** Photocatalytic H<sub>2</sub> evolution over CdS, CdS-EGR with different weight ratios of EGR (A), and photocatalytic H<sub>2</sub> evolution over CdS, CdS-RGO with different weight ratios of RGO (B). Time-online photoactivity comparison of photocatalytic H<sub>2</sub> evolution activities over CdS, CdS-2%RGO and CdS-2%EGR (C). Recycling photoactivity test over CdS, CdS-2%RGO and CdS-2%EGR (D). Note that the error bars represent the photoactivity standard deviation values calculated from triplicate experiments.

blank CdS, while CdS-2%EGR displays the highest photocurrent transient response under visible light irradiation, suggesting that the lifetime of photogenerated charge carriers achieved on CdS-2%EGR is significantly enhanced [44,57]. In addition, we can observe a photocurrent decay upon light irradiation, which can be attributed to recombination of photogenerated electron-hole pairs in the process of illumination [60–62]. Fig. 5B shows the EIS Nyquist plots of the electrodes made of blank CdS, CdS-2%RGO and CdS-2%EGR under visible light irradiation. It is clearly seen that the three electrode materials all show semicycles at high frequencies. The smallest arc radius of the EIS Nyquist plot of CdS-2%EGR implies that it has the fastest interfacial electron transfer than that of blank CdS and CdS-2%RGO [63,64]. Fig. 5C displays the linear sweep voltammetry curves of CdS, CdS-2%RGO and CdS-2%EGR. The cathodic current density obtained over the CdS-2%EGR electrode is higher than that over CdS-2%RGO and blank CdS, which is consistent with the result that EGR can promote the photoactivity of reduction of water to H<sub>2</sub> more effectively than RGO [65]. The PL spectrum, which is often employed to study surface processes involving the photoexcited electron transfer and recombination has been performed [11,66]. As depicted in Fig. 5D, all of the samples show PL signals with similar curves. Notably, after the decoration of graphene, the PL intensity of the CdS-graphene composites obviously diminishes compared to that of bare CdS, which is attributed to the fact that graphene can act as a sink to trap or shuttle the photogenerated electrons from CdS, thus retarding the undesirable recombination process of the electron-hole pairs [9,67]. Furthermore, the integration of EGR with semiconductor CdS results in a strongest quenching degree of

PL intensity, suggesting that the recombination of photogenerated electron-hole pairs over CdS-2%EGR is most efficiently inhibited among the three samples [44,58,68].

Fig. S11 shows the nitrogen adsorption-desorption isotherm results of CdS, CdS-2%RGO and CdS-2%EGR samples. The Brunauer-Emmett-Teller (BET) surface area of these samples is determined to be *ca.* 3.95 m<sup>2</sup> g<sup>-1</sup>, 11.31 m<sup>2</sup> g<sup>-1</sup>, and 5.36 m<sup>2</sup> g<sup>-1</sup>, respectively, following the order of CdS-2%RGO > CdS-2%EGR > CdS. However, the photoactivity order of these samples is CdS-2%EGR > CdS-2%RGO > CdS. Therefore, it is reasonable to infer that the surface area is not the primary reason accounting for the significant photoactivity difference between CdS, CdS-2%RGO and CdS-2%EGR. On the contrary, the different separation and transfer efficiency caused by the difference of electric conductivity between EGR and RGO are the key and predominant factors that determine the photoactivity difference between CdS-2%RGO and CdS-2%EGR. Thus far, the tentative reaction mechanisms for photocatalytic H<sub>2</sub> evolution from water over CdS-2%RGO and CdS-2%EGR have been proposed, as schematically illustrated in Fig. 5E,F. Upon visible light irradiation, the electrons in the valence band (VB) of CdS are photoexcited to the conduction band (CB), leaving holes in the VB. The intimate interfacial contact and matched energy level favor the vectorial transfer of photogenerated electrons in the CB of CdS to graphene, while the holes are consumed by the scavenger of lactic acid. Graphene as co-catalysts improves the separation and transfer efficiency of photogenerated charge carriers, thereby increasing the overall photocatalytic H<sub>2</sub> evolution efficiency of composites. As for the different photocatalytic performance, it is mainly

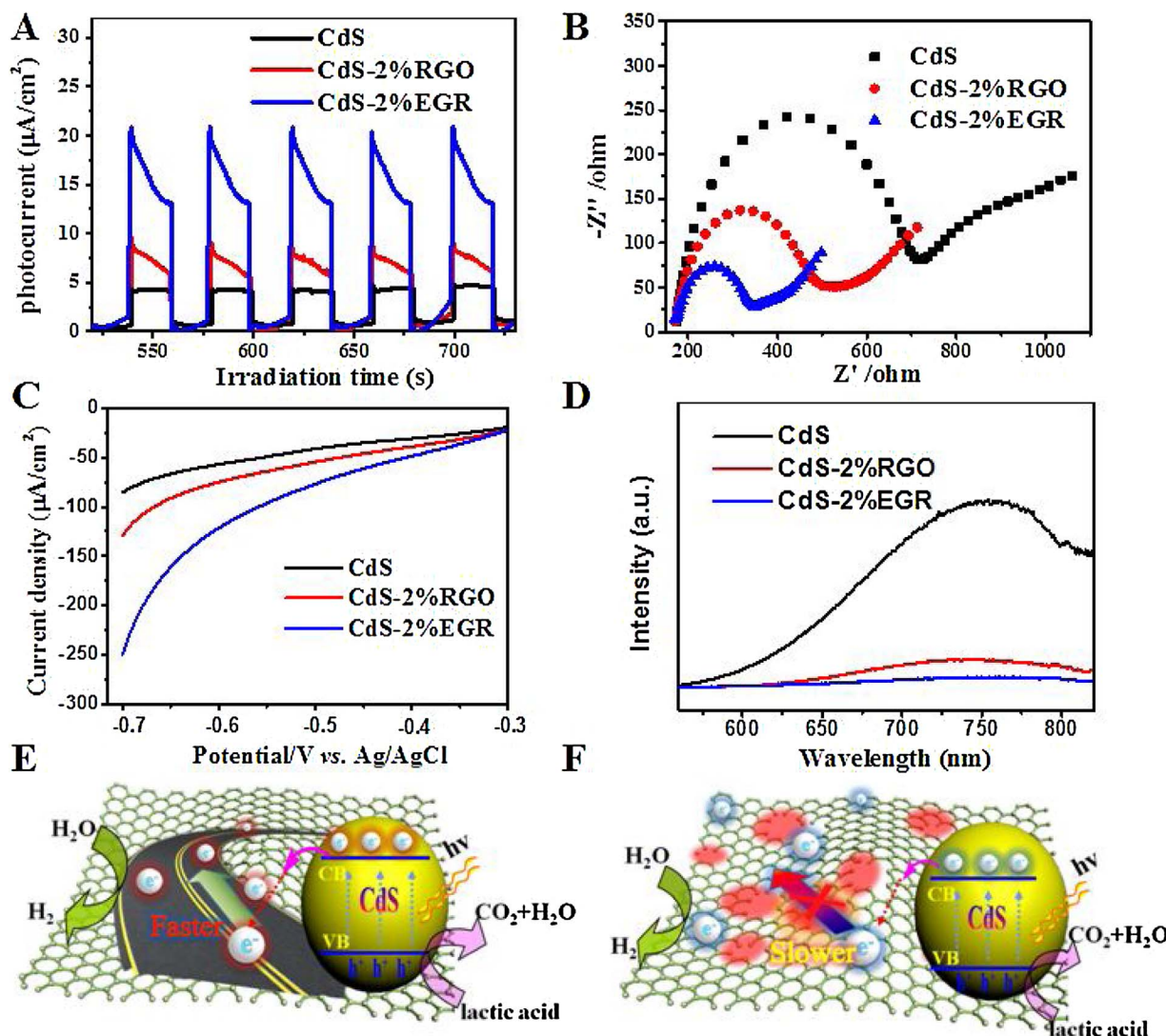


**Fig. 5.** Transient photocurrent responses (A), electrochemical impedance spectroscopy Nyquist plots (B), polarization curves (C), and PL spectra with an excitation wavelength of 420 nm (D) of CdS, CdS-2%RGO, and CdS-2%EGR. Schematic illustration for the photocatalytic H<sub>2</sub> evolution over the CdS-EGR (E) and CdS-RGO (F) under visible light irradiation.

caused by the structural and electronic differences between RGO and EGR. The EGR sheet with significantly enhanced electrical conductivity as compared to RGO implies that it can provide a longer mean free path for photoexcited energetic electrons to diffuse farther [44,58], which more efficiently inhibits the recombination of electron-hole pairs and increases their likelihood of interaction with proton to produce H<sub>2</sub>. In contrast, intrinsic large population of structural defects result in considerable disruption of the 2D  $\pi$ -conjugation of the electronic structure of RGO, leading to its much lower electrical conductivity and charge carrier mobility than EGR. Consequently, the CdS-EGR composites display higher visible light photocatalytic H<sub>2</sub> production activity than CdS-RGO counterparts.

#### 4. Conclusion

In summary, we have reported a conceptual study of improving the photocatalytic performance of CdS-graphene composites *via* rational utilization of the highly conductive commercial EGR, which is manufactured on a large scale *via* a high-shear exfoliation process in liquid-phase. A simple surface modification *via* using surfactant of SDS has been adopted to resolve the low solution processability of EGR, which endows the EGR surface with additional hydrophilic functional groups, thus making SDS-modified EGR well dispersed in aqueous phase and

negatively charged. In addition, the electrostatic self-assembly strategy guarantees the intimate interface contact between graphene and CdS. The significantly improved electrical conductivity of EGR as compared to RGO results in the more efficient separation and transfer of photo-generated charge carriers in CdS-EGR composite than CdS-RGO counterpart under visible light irradiation, which consequently results in the much higher photoactivity of CdS-EGR than CdS-RGO for H<sub>2</sub> evolution. It is anticipated that our current work would inform ongoing efforts to explore rational utilization of highly conductive commercial graphene to design more efficient graphene-semiconductor photocatalysts for practical applications.

#### Acknowledgments

The support from the National Natural Science Foundation of China (U1463204, 20903023 and 21173045), the Award Program for Minjiang Scholar Professorship, the Natural Science Foundation (NSF) of Fujian Province for Distinguished Young Investigator Rolling Grant (2017J07002), the Independent Research Project of State Key Laboratory of Photocatalysis on Energy and Environment (NO. 2014A05), the 1st Program of Fujian Province for Top Creative Young Talents, and the Program for Returned High-Level Overseas Chinese Scholars of Fujian province is gratefully acknowledged.

## Appendix A. Supplementary data

Supplementary data associated with this article can be found, in the online version, at <http://dx.doi.org/10.1016/j.apcatb.2017.10.021>.

## References

- [1] N. Zhang, M.-Q. Yang, S. Liu, Y. Sun, Y.-J. Xu, Chem. Rev. 115 (2015) 10307–10377.
- [2] H. Zhang, X. Lv, Y. Li, Y. Wang, J. Li, ACS Nano 4 (2010) 380–386.
- [3] J. Liu, H. Bai, Y. Wang, Z. Liu, X. Zhang, D.D. Sun, Adv. Funct. Mater. 20 (2010) 4175–4181.
- [4] J.S. Lee, K.H. You, C.B. Park, Adv. Mater. 24 (2012) 1084–1088.
- [5] Q. Li, B. Guo, J. Yu, J. Ran, B. Zhang, H. Yan, J.R. Gong, J. Am. Chem. Soc. 133 (2011) 10878–10884.
- [6] Q. Xiang, J. Yu, M. Jaroniec, J. Am. Chem. Soc. 134 (2012) 6575–6578.
- [7] Y. Zhang, N. Zhang, Z.-R. Tang, Y.-J. Xu, ACS Nano 6 (2012) 9777–9789.
- [8] Y. Zhang, Z.-R. Tang, X. Fu, Y.-J. Xu, ACS Nano 4 (2010) 7303–7314.
- [9] S. Thakur, T. Kshetri, N.H. Kim, J.H. Lee, J. Catal. 345 (2017) 78–86.
- [10] M.-Q. Yang, N. Zhang, M. Pagliaro, Y.-J. Xu, Chem. Soc. Rev. 43 (2014) 8240–8254.
- [11] N. Zhang, M.-Q. Yang, Z.-R. Tang, Y.-J. Xu, ACS Nano 8 (2014) 623–633.
- [12] T.-H. Yang, Y.-W. Harn, L.-D. Huang, M.-Y. Pan, W.-C. Yen, M.-C. Chen, C.-C. Lin, P.-K. Wei, Y.-L. Chueh, J.-M. Wu, J. Catal. 329 (2015) 167–176.
- [13] F. Chen, W. An, L. Liu, Y. Liang, W. Cui, Appl. Catal. B 217 (2017) 65–80.
- [14] M. Hamandi, G. Berhault, C. Guillard, H. Kochkar, Appl. Catal. B 209 (2017) 203–213.
- [15] T. Xu, L. Zhang, H. Cheng, Y. Zhu, Appl. Catal. B 101 (2011) 382–387.
- [16] D.P. Kumar, S. Hong, D.A. Reddy, T.K. Kim, Appl. Catal. B 212 (2017) 7–14.
- [17] Y. Lei, C. Yang, J. Hou, F. Wang, S. Min, X. Ma, Z. Jin, J. Xu, G. Lu, K.-W. Huang, Appl. Catal. B 216 (2017) 59–69.
- [18] X. Li, J. Yu, S. Wageh, A.A. Al-Ghamdi, J. Xie, Small 12 (2016) 6640–6696.
- [19] Q. Xiang, B. Cheng, J. Yu, Angew. Chem. Int. Ed. 54 (2015) 11350–11366.
- [20] G. Xie, K. Zhang, B. Guo, Q. Liu, L. Fang, J.R. Gong, Adv. Mater. 25 (2013) 3820–3839.
- [21] X. Gong, W.Y. Teoh, J. Catal. 332 (2015) 101–111.
- [22] K. Ojha, T. Debnath, P. Maity, M. Makkar, S. Nejati, K.V. Ramanujachary, P.K. Chowdhury, H.N. Ghosh, A.K. Ganguli, J. Phys. Chem. C 121 (2017) 6581–6588.
- [23] Z. Tian, N. Yu, Y. Cheng, Z. Wang, Z. Chen, L. Zhang, Mater. Lett. 194 (2017) 172–175.
- [24] F. Banhart, J. Kotakoski, A.V. Krasheninnikov, ACS Nano 5 (2010) 26–41.
- [25] A. Lerf, H. He, M. Forster, J. Klinowski, J. Phys. Chem. B 102 (1998) 4477–4482.
- [26] K.-Q. Lu, N. Zhang, C. Han, F. Li, Z. Chen, Y.-J. Xu, J. Phys. Chem. C 120 (2016) 27091–27103.
- [27] D.R. Dreyer, S. Park, C.W. Bielawski, R.S. Ruoff, Chem. Soc. Rev. 39 (2010) 228–240.
- [28] X. Jiang, J. Nisar, B. Pathak, J. Zhao, R. Ahuja, J. Catal. 299 (2013) 204–209.
- [29] C. Mattevi, H. Kim, M. Chhowalla, J. Mater. Chem. 21 (2011) 3324–3334.
- [30] A. Reina, X. Jia, J. Ho, D. Nezich, H. Son, V. Bulovic, M.S. Dresselhaus, J. Kong, Nano Lett. 9 (2008) 30–35.
- [31] Y.L. Zhong, Z. Tian, G.P. Simon, D. Li, Mater. Today 18 (2015) 73–78.
- [32] Q. Bao, H. Zhang, Y. Wang, Z. Ni, Y. Yan, Z.X. Shen, K.P. Loh, D.Y. Tang, Adv. Funct. Mater. 19 (2009) 3077–3083.
- [33] Y.T. Liang, B.K. Vijayan, K.A. Gray, M.C. Hersam, Nano Lett. 11 (2011) 2865–2870.
- [34] Y. Hernandez, V. Nicolosi, M. Lotya, F.M. Blighe, Z. Sun, S. De, I.T. McGovern, B. Holland, M. Byrne, Y.K. GunKo, J.J. Boland, P. Niraj, G. Duesberg, S. Krishnamurthy, R. Goodhue, J. Hutchison, V. Scardaci, A.C. Ferrari, J.N. Coleman, Nat. Nanotechnol. 3 (2008) 563–568.
- [35] Y. Zhang, N. Zhang, Z.-R. Tang, Y.-J. Xu, Phys. Chem. Chem. Phys. 14 (2012) 9167–9175.
- [36] H. Feng, Y. Wu, J. Li, Small 10 (2014) 2233–2238.
- [37] R. Ciriminna, N. Zhang, M.-Q. Yang, F. Meneguzzo, Y.-J. Xu, M. Pagliaro, Chem. Commun. 51 (2015) 7090–7095.
- [38] K.R. Paton, E. Varrla, C. Backes, R.J. Smith, U. Khan, A. O'Neill, C. Boland, M. Lotya, O.M. Istrate, P. King, Nat. Mater. 13 (2014) 624–630.
- [39] M.P. Bailey, Chem. Eng. 121 (2014) 13–17.
- [40] Z. Chen, S. Liu, M.-Q. Yang, Y.-J. Xu, ACS Appl. Mater. Interfaces 5 (2013) 4309–4319.
- [41] G. Lin, J. Zheng, R. Xu, J. Phys. Chem. C 112 (2008) 7363–7370.
- [42] M.-Q. Yang, C. Han, Y.-J. Xu, J. Phys. Chem. C 119 (2015) 27234–27246.
- [43] M.-Q. Yang, Y.-J. Xu, J. Phys. Chem. C 117 (2013) 21724–21734.
- [44] M.-Q. Yang, C. Han, N. Zhang, Y.-J. Xu, Nanoscale 7 (2015) 18062–18070.
- [45] N. Zhang, Y. Zhang, X. Pan, X. Fu, S. Liu, Y.-J. Xu, J. Phys. Chem. C 115 (2011) 23501–23511.
- [46] Y. Zhang, Z.-R. Tang, X. Fu, Y.-J. Xu, ACS Nano 5 (2011) 7426–7435.
- [47] W. Zhang, Y. Wang, Z. Wang, Z. Zhong, R. Xu, Chem. Commun. 46 (2010) 7631–7633.
- [48] B. Weng, M.-Q. Yang, N. Zhang, Y.-J. Xu, J. Mater. Chem. A 2 (2014) 9380–9389.
- [49] O. Parlak, A. Tiwari, A.P.F. Turner, A. Tiwari, Biosens. Bioelectron. 49 (2013) 53–62.
- [50] S. Zhou, D. Wei, H. Shi, X. Feng, K. Xue, F. Zhang, W. Song, Talanta 107 (2013) 349–355.
- [51] X. Gong, G. Liu, Y. Li, D.Y.W. Yu, W.Y. Teoh, Chem. Mater. 28 (2016) 8082–8118.
- [52] S. Zinadini, A.A. Zinatizadeh, M. Rahimi, V. Vatanpour, H. Zangeneh, J. Membr. Sci. 453 (2014) 292–301.
- [53] J.M. Lee, E.K. Mok, S. Lee, N.S. Lee, L. Debbichi, H. Kim, S.J. Hwang, Angew. Chem. Int. Ed. 55 (2016) 8546–8550.
- [54] T. Kuila, S. Bose, A.K. Mishra, P. Khanra, N.H. Kim, J.H. Lee, Prog. Mater. Sci. 57 (2012) 1061–1105.
- [55] L.J. Cote, F. Kim, J. Huang, J. Am. Chem. Soc. 131 (2009) 1043–1049.
- [56] S. Stankovich, D.A. Dikin, R.D. Piner, K.A. Kohlhaas, A. Kleinhammes, Y. Jia, Y. Wu, S.T. Nguyen, R.S. Ruoff, Carbon 45 (2007) 1558–1565.
- [57] F.-X. Xiao, J. Miao, B. Liu, J. Am. Chem. Soc. 136 (2014) 1559–1569.
- [58] N. Zhang, M.-Q. Yang, Z.-R. Tang, Y.-J. Xu, J. Catal. 303 (2013) 60–69.
- [59] Z. Chen, Y.-J. Xu, ACS Appl. Mater. Interfaces 5 (2013) 13353–13363.
- [60] Q. Xiang, J. Yu, M. Jaroniec, Nanoscale 3 (2011) 3670–3678.
- [61] Y. Lei, R. Li, F. Chen, J. Xu, J. Mater. Sci. Mater. Electron. 25 (2014) 3057–3061.
- [62] J. Zhang, J. Yu, M. Jaroniec, J.R. Gong, Nano Lett. 12 (2012) 4584–4589.
- [63] B. Qiu, M. Xing, J. Zhang, J. Am. Chem. Soc. 136 (2014) 5852–5855.
- [64] D. Wang, D. Choi, J. Li, Z. Yang, Z. Nie, R. Kou, D. Hu, C. Wang, L.V. Saraf, J. Zhang, I.A. Aksay, J. Liu, ACS Nano 3 (2009) 907–914.
- [65] M.-Q. Yang, Y.-J. Xu, W. Lu, K. Zeng, H. Zhu, Q.-H. Xu, G.W. Ho, Nat. Commun. 8 (2017) 14224.
- [66] W. Tu, Y. Zhou, Q. Liu, Z. Tian, J. Gao, X. Chen, H. Zhang, J. Liu, Z. Zou, Adv. Funct. Mater. 22 (2012) 1215–1221.
- [67] B. Weng, Y.-J. Xu, ACS Appl. Mater. Interfaces 7 (2015) 27948–27958.
- [68] X. Yu, R. Du, B. Li, Y. Zhang, H. Liu, J. Qu, X. An, Appl. Catal. B 182 (2016) 504–512.